Spring 5-10-2023

Computational Analysis of Steady Hypersonic Flow Fields of NASA Benchmark Geometries Utilizing ANSYS Fluent

Aidan Murphy
Washington University in St. Louis

Recommended Citation

Murphy, Aidan, "Computational Analysis of Steady Hypersonic Flow Fields of NASA Benchmark Geometries Utilizing ANSYS Fluent" (2023). *McKelvey School of Engineering Theses & Dissertations*. 821.
https://openscholarship.wustl.edu/eng_etds/821

WASHINGTON UNIVERSITY IN ST. LOUIS

McKelvey School of Engineering
Department of Mechanical Engineering & Materials Science

Thesis Examination Committee
Ramesh K. Agarwal, Chair
Swami Karunamoorthy
David Peters

Computational Analysis of Steady Hypersonic Flow Fields of NASA Benchmark Geometries Utilizing ANSYS Fluent

by
Aidan Robert Murphy

A thesis presented to
the McKelvey School of Engineering
of Washington University in
partial fulfillment of the
requirements for the degree
of Master of Science

May 2023
St. Louis, Missouri

Table of Contents

List of Figures

List of Tables

Acknowledgments

I would like to extend my utmost appreciation in acknowledging my research advisor, Dr. Ramesh K. Agarwal, for his continuous support and determination in ensuring my success as an accomplished researcher in the field of Computational Fluid Dynamics. His assistance and encouragement have allowed me to pursue complex hypersonic problems and continue the growth of my passion for aerodynamics.

I would also like to acknowledge Dr. David Peters and Dr. Swami Karunamoorthy for agreeing to be the thesis committee members and reading this thesis.

Lastly, I would like to thank Missouri NASA Space Grant for financial support.

Aidan R Murphy

Washington University in St. Louis

May 2023

Dedicated to my parents.

ABSTRACT OF THE THESIS

Computational Analysis of Steady Hypersonic Flow Fields of NASA Benchmark Geometries Utilizing ANSYS Fluent

by

Aidan Robert Murphy

Master of Science in Aerospace Engineering

Washington University in St. Louis, 2023

Professor Ramesh K. Agarwal, Chair

The Hypersonic International Flight Research Experimentation (HIFiRE) program explores and advances hypersonic aerospace systems by developing a multitude of test flight geometries and conducting experimental test flights to obtain data for use in validation of computational models and results. This study focuses on computational validation of heat flux, and calculation of static pressure profiles, skin friction coefficient profiles, and flow contours. The flow fields studied are for Mach number 7.18 and angles of attack (α) of 0° & 2°. These flow fields include many compressible flow features such as an expansion wave at the intersection of the cone and flat cylindrical section, an oblique shock wave at the cylinder and flare connection point, and a detached bow shock at the tip of the geometry. These flow features are present in the experimental test flight data as well as in ground test studies conducted in the CALSPAN–University of Buffalo Research Center's LENS I facility along with computational results presented at the 2022 High-Fidelity CFD Workshop. Computations are performed using the Reynolds-Averaged Navier-Stokes (RANS) equations with one-equation Spalart-Allmaras (SA) turbulence model in ANSYS Fluent with suitable boundary conditions which give results for non-dimensionalized heat flux and static pressure profiles that closely match the computational results presented at the 2022 High-Fidelity CFD Workshop within 5% for $\alpha = 2°$.

Hypersonic flow past the Blottner Sphere is another benchmark test case recently proposed for verification and validation of CFD codes in the High-Fidelity CFD Workshop organized in 2022 by NASA Langley Research Center in association with AIAA. Investigations into Blottner Sphere date back to the early 1960s and it has continued to be a problem of great interest in the field of high-speed computational and experimental fluid dynamics. This paper also focuses on the computation of steady laminar hypersonic flow past the Blottner Sphere using the three-dimensional compressible Navier-Stokes equations with suitable boundary conditions in ANSYS Fluent. Results are obtained for surface heating and pressure on the sphere at Mach 5.0 freestream. The simulation results correctly predict the separated bow shock upstream of the sphere along with the shock detachment distance from the stagnation point. The computed normalized pressure and heat flux on the surface are compared with the results obtained by 2022 High-Fidelity CFD Workshop participants.

Chapter 1: Introduction

This chapter provides background information on the field of Computational Fluid Dynamics (CFD) and its application to various problems with hypersonic freestream conditions. Furthermore, discussion of the motivation behind computational simulation of different geometries in a steady hypersonic flow field is included. Simulations of different hypersonic benchmark test cases offer insight into these complex problems and the research covered within this thesis provides computational results that add to the progress in field of hypersonic turbulence modeling. This section also details the scope of this thesis.

1.1 Motivation and Background

The field of Computational Fluid Dynamics (CFD) is becoming increasingly more important as the years go by due to the affordability of computational simulations compared to traditional experimentation methods of solving fluid flow problems. CFD is an efficient and cost-effective tool to analyze and solve problems involving the flow of fluids. The most common CFD methods involve solving the Navier-Stokes Equations, combined with the energy equation and continuity equation in order to model viscous flow within a specified domain (either internal or external). The Navier-Stokes equations are systems of highly non-linear partial differential equations that cannot be solved analytically for complex three-dimensional geometries and therefore necessarily require numerical methods for their solution. Several simplifications can be made to the Navier-Stokes equations which can yield to the Euler equations (by removing the viscous terms) or the full potential equations (by additionally removing the vorticity terms). CFD employs geometry modeling and grid generation to break a complex problem into a multitude of small problems that can be solved simultaneously. For any given fluid flow problem, an appropriate physical model with governing equations and boundary conditions is needed to solve a given problem.

For solving the Navier-Stokes equations for turbulent fluid motion, there have been primarily three approaches known as the Reynolds-Averaged Navier-Stokes (RANS) equations, Large-Eddy Simulation (LES) and Direct Numerical Simulation (DNS). Among these, the most commonly used method in industrial applications is RANS equations whose solution requires a turbulence model to model the turbulent stresses in the equations in order to achieve closure of the equations. RANS equations are time averaged equations that separate the mean part of the bulk flow from the fluctuating term whose time-averaging leads to the generation of the 'Reynolds Stresses' and in turn, the 'Closure Problem.' Due to this reason, the 'Reynolds Stresses' must be modeled in order to be able to solve a fluid flow problem using RANS equations. This leads to the need for turbulence models and importance of 'Turbulence Modeling.'

The most common RANS turbulence models are linear eddy viscosity models in which the 'Reynolds Stresses' are modeled with a linear constitutive relation known as the 'Boussinesq hypothesis.' Within these linear eddy viscosity models the most commonly used models are algebraic (0-equation), one-equation, or two-equation models. This thesis employs the most commonly used (in commercial and industrial applications) one-equation turbulence model known as the Spalart-Allmaras (SA) turbulence model.

Many CFD methods focus on flow regimes that are incompressible or subsonic, where the velocity of the flow is slower than speed of sound. The focus of this thesis is on hypersonic flow fields, which are generally categorized as flows with free stream conditions that are approximately five times or greater than the speed of sound in the fluid. This leads to many challenges with the CFD methods due to the presence of shock waves and high heating in the boundary layer on the aerodynamic body.

Another focus of this thesis is on laminar flow simulation of the three-dimensional compressible Navier-Stokes equations with the continuity and energy equation. The goal of this investigation is to determine the computational domain and mesh requirements for accurate and efficient simulation of pressure and heat flux on the body. This problem is of interest since the flow is laminar on the leading edge of many hypersonic bodies such as space shuttle as well as blunt reentry bodies.

1.2 Scope of the Thesis

The goal of this research is to provide further insight and advance results in the field of steady hypersonic CFD. This work builds on the first AIAA High Fidelity CFD workshop that took place in January 2022 with participants working on complex steady hypersonic flow benchmark problems in an attempt to obtain information on the ability of different CFD codes to converge to a similar result on a prescribed mesh and boundary conditions as well as to evaluate the accuracy of results obtained from different CFD codes. Additional simulations and results are included to provide further insight into these problems. A title and a summary of each chapter are given below:

Chapter 2: Introduction to Hypersonic Flow and Turbulence Modeling: This chapter introduces the common methods for steady hypersonic flow simulations in CFD. Hypersonic flow introduces many complexities within a flow field including fluid compressibility effects, strong shock waves, and flow expansion. Aerodynamic heating becomes very important in this flow regime due to the large surface heating that is imparted onto an aerodynamic body. A brief introduction to hypersonic flow and the CFD methods utilized in this thesis is also presented in this section.

Chapter 3: Computational Analysis of the HIFiRE-1 Hypersonic Test Model: Simulation of the HIFiRE-1 test model at 2° angle of attack is compared to the results of the High-Fidelity CFD Workshop participants along with information on the skin friction coefficient that is not included in the workshop results. Further simulation results are presented for an angle of attack of 0° along with Mach contours that are correlated to results from experimental ground test studies. This chapter describes the comparison of the present simulation results to the workshop participants as well as providing further information for simulations at 0° angle of attack.

Chapter 4: Laminar Steady Hypersonic Flow past Blottner Sphere: Three dimensional Navier-Stokes equations are simulated over the benchmark geometry known as the Blottner Sphere. This chapter summarizes the steady laminar hypersonic flow results and provides a comparison of the present results with those of the High-Fidelity CFD Workshop participants.

Chapter 5: Summary: This chapter focuses on the key results from each of the previous chapters and summarizes the important findings from this work.

Chapter 2: Introduction to Hypersonic Flow and Turbulence Modeling

2.1 Introduction to Hypersonic Flow

Depending upon the freestream flow conditions, there are different flow regimes that can be observed in external flow past a body. The categorization of these flow regimes is generally defined by the Mach number (V/a), which relates the speed of sound “a” in a flow media to the velocity V of the freestream. When Mach number is greater than 1, the flow is defined as supersonic or hypersonic. Although it is not a strict definition, the flow is generally considered as hypersonic if the Mach number is greater than 5; it is generally characterized by the molecular dissociation and ionization that occurs in the flow at high speeds. Hypersonic speed introduces many complexities in the flow features which may include flow expansion region, shock waves, transitional and turbulent boundary layers and wakes with large surface heating [1]. In order to accurately simulate the hypersonic flows, one needs to have a deeper understanding of compressible flows and the impact of compressibility on Reynolds-Averaged Navier-Stokes (RANS) e.g. Favre equations and the turbulence models. One of the most important aspects of hypersonic flow is the significant increase in temperature resulting in chemically reacting flow fields in highly compressible flow [1]. Hypersonic flow classification relies on many of the attributes described above and some specific features of this flow regime can be seen in test cases described in both Chapter 3 and 4.

2.2 Introduction to Turbulence Modeling

In general, a typical fluid flow exhibits one of the three types of behavior: laminar, transitional, or turbulent. Laminar flow is considered the simplest flow behavior since there is no mixing occurring between the fluid layers moving along streamlines in the flow and the fluid particles follow well defined path lines [2]. Turbulent flow is categorized by random and irregular fluctuations in the flow resulting in the mixing in the flow and turbulent eddies [3]. Transitional flow is the flow regime that is in between the laminar and the turbulent, where the onset of turbulent flow characteristics begins after the laminar flow regime [2]. Due to the complexity of turbulence, analytical and theoretical calculations of turbulent flow are exceedingly difficult and have not been feasible leading to the necessity of models that capture turbulence properties. Most flows in the real-world are turbulent and therefore there is need to develop models to characterize their behavior.

As previously discussed in Chapter 1, there are many mathematical and numerical approaches for capturing the turbulent flow in a given application of interest which include RANS, LES, and DNS. The RANS equations combined with a turbulence model are commonly utilized in industry for solving the complex turbulent flow problems whose solution is needed using CFD technology for design and optimization of a product in a timely and cost effective manner. The main source of inaccuracy in RANS simulation occurs from a turbulence model employed. Majority of the turbulence models are the so called linear eddy viscosity models which are based on the ‘Boussinesq hypothesis’ which postulates that the turbulent or Reynolds stresses are proportional to strain rate tensor and the proportionality constant is the turbulent eddy viscosity of the flow. These models are classified as algebraic (0-equation), one-equation, two-equation model, or full Reynolds-stress models in the literature [3]. Many of these models are incorporated into commercial CFD codes such as ANSYS Fluent and COMSOL and open-source code OpenFOAM along with many other academic or government labs developed codes.

Before covering more information on turbulence modeling, it is important to note that part of this work involves simulating the three-dimensional laminar compressible Navier-Stokes equations. For the problem covered in Chapter 4, a laminar viscous solution is obtained by solving the compressible Navier-Stokes equations while neglecting any turbulent parameters. This is done to simulate laminar flow due to the geometry being very small and having a stagnation point that forces the flow to become laminar. Transition to turbulence would occur if the geometry was extended; however, the laminar flow assumption is valid for the test case considered.

Among all the turbulence models, the one-equation Spalart-Allmaras model is the most widely used model for simulation of aerodynamic flows. This model is employed in this thesis and is briefly described here. This model was assembled using empiricism and arguments of dimensional analysis. The transport equation for turbulent kinematic viscosity is given as Eq. (1) which includes a destruction term. The fine tuning of various coefficients was completed based on correlations to experimental data. Equation (2.1) depicts the non-conservative form for the transport of kinematic eddy viscosity in the flow [4]:

$$\frac{\partial \hat{\nu}}{\partial t} + u_j \frac{\partial \hat{\nu}}{\partial x_j} = c_{b1}(1 - f_{t2})\hat{S}\hat{\nu} - \left[c_{w1} f_w - \frac{c_{b1}}{\kappa^2} f_{t2}\right]\left(\frac{\hat{\nu}}{d}\right)^2 + \frac{1}{\sigma}\left[\frac{\partial}{\partial x_j}\left((\nu + \hat{\nu})\frac{\partial \hat{\nu}}{\partial x_j}\right) + c_{b2}\frac{\partial \hat{\nu}}{\partial x_j}\frac{\partial \hat{\nu}}{\partial x_j}\right] \quad (2.1)$$

The SA model has been validated and verified for a wide variety of fluid flow problems and due to its implementation into many commercial CFD codes, this model has become widely popular.

2.3 References

[1] Anderson, J. D., *Modern compressible flow: With historical perspective*, Boston: McGraw-Hill Education, 2021.

[2] Munson, B. R., Okiishi, T. H., Huebsch, W. W., and Rothmayer, A. P., *Fundamentals of Fluid Mechanics*, Hoboken, NJ: John Wiley et Sons, Inc., 2013.

[3] White, F. M., *Viscous Fluid Flow*, New York, NY: McGraw-Hill Higher Education, 2006.

[4] Spalart, P. R., and Allmaras, S. R., “A One-Equation Turbulence Model for Aerodynamic Flows,” AIAA Conference Paper AIAA-92-0439, 30th Aerospace Sciences Meeting and Exhibit, Reno, NV, 1992. https://doi.org/10.2514/6.1992-439.

Chapter 3: Computational Analysis of the HIFiRE-1 Hypersonic Test Model

3.1 Introduction

The Hypersonic International Flight Research Experimentation (HIFiRE) program consists of a multitude of flight tests that aim to explore and advance hypersonic aerospace systems. HIFiRE-1 was developed to obtain information about turbulent separated flow, boundary-layer transition, and shock wave/boundary-layer interaction in high-speed flow [1]. HIFiRE-1 has been adopted as one of the test cases for the High-Fidelity CFD Workshop organized by the NASA Langley Research Center in association with AIAA SciTech Forum in January 2022. This test case explores the steady state CFD modeling of the HIFiRE-1 geometry in hypersonic flow at $\alpha = 2°$ to evaluate the ability of different flow solvers to converge to the same solution when the mesh is refined [2]. The HIFiRE-1 geometry consists of an axisymmetric slightly blunt nose with 7° cone attached to a flat cylindrical section followed by a flare at 33° and ending with a smaller flat cylindrical section. Figure 3.1 shows this geometry as an axisymmetric half section of the full geometry.

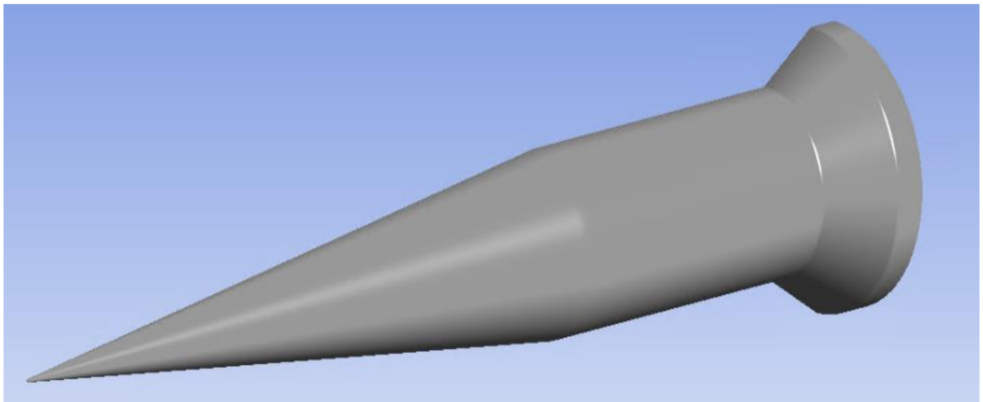

Figure 3.1 HIFiRE-1 geometry.

The HIFiRE-1 flight geometry dimensions are given in Fig. 3.2. Note that the labelled relevant dimensions differ slightly from Fig. 3.2 near the flare section (including the location and angle of the flare) since there were additional manufactured blunted noses and flare sections that could be added to change the overall geometry during testing [1].

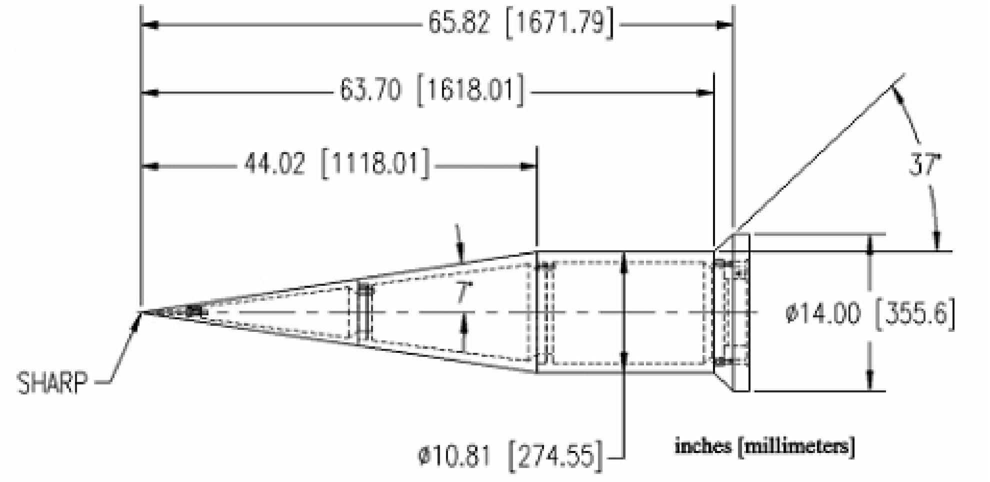

Figure 3.2 HIFiRE-1 geometry with relevant dimensions in imperial and metric units [1].

The HIFiRE-1 project is of great interest since there are plentiful resources for in-flight data collection as well as computational results that explore different areas of this hypersonic flow problem. Further analysis of hypersonic flow fields allows for a deeper understanding of the geometric impact of flow induced heat flux on the body. The ongoing joint efforts of this type of analysis (both experimental and computational) will aid in expanding the current hypersonic aerospace systems' knowledge base. Not only have these advancements taken place with the HIFiRE-1 geometry, but the whole HIFiRE program provides a deeper understanding of the practicalities of hypersonic flight.

Experimental flight test results for the HIFiRE-1 program have been published in the AIAA Journal of Spacecraft and Rockets which provide detailed heating and pressure data over the full-scale HIFiRE-1 flight geometry. The goal of HIFiRE-1 experiment was to collect accurate flight data that can be utilized by CFD codes for validation of boundary-layer transition, turbulent separated flow, and shock/boundary-layer interaction on the geometry [1]. The results have also been published to compare the experimental test flight data to the computational analyses using CFD codes and a parabolized stability equation code for analyzing the boundary layer transition. The published CFD results compare the flight test data at $\alpha = 0°$ for laminar heating, transition onset, turbulent heating, and separation on the turbulent flare [3].

The analysis in this thesis focuses on CFD simulation results at $\alpha = 0°$ and 2°, $M = 7.18$ and a freestream Reynolds number $Re = 10.213 \times 10^6$/ m [2]. Simulations for both angles of attack for the HIFiRE-1 geometry are conducted to obtain results that can be compared to the computational results from the 2022 High-Fidelity CFD Workshop as well as the experimental analysis conducted at the CALSPAN–University of Buffalo Research Center's LENS I facility in Buffalo, New York. These flow conditions are similar to the flow conditions imposed during "Condition B" of the experimental and computational analysis completed in Refs. [1] and [3] and are the same flow conditions dictated by the High-Fidelity CFD Workshop [2].

3.2 Computational Mesh

As part of the High-Fidelity CFD Workshop, there are multiple structured and unstructured grids given for the HIFiRE-1 geometry which include meshes for the overall geometry and individual meshes for the cone section [2]. An example of the provided structured mesh for the full geometry employed in the present computational analysis is a mesh around a three-dimensional cross-section along the x-y plane as shown in Fig. 3.3. The provided cgns mesh file was imported into ANSYS ICEM CFD [4]. Each full geometry mesh has flow domain elements and elements with labels for the inlet, outlet, symmetry plane, and the wall (i.e., the surface geometry of HIFiRE-1). In Fig. 3.3, the exterior red portion is the inlet domain, the orange region on the right is the outlet, the green elements correspond to the wall, the blue portion is the symmetry plane, and the purple elements in the interior of the mesh are the flow domain elements. The flow domain consists of hexahedron elements with 8 vertices, while the labeled exterior domains of the mesh consist of quadrilateral elements with 4 vertices.

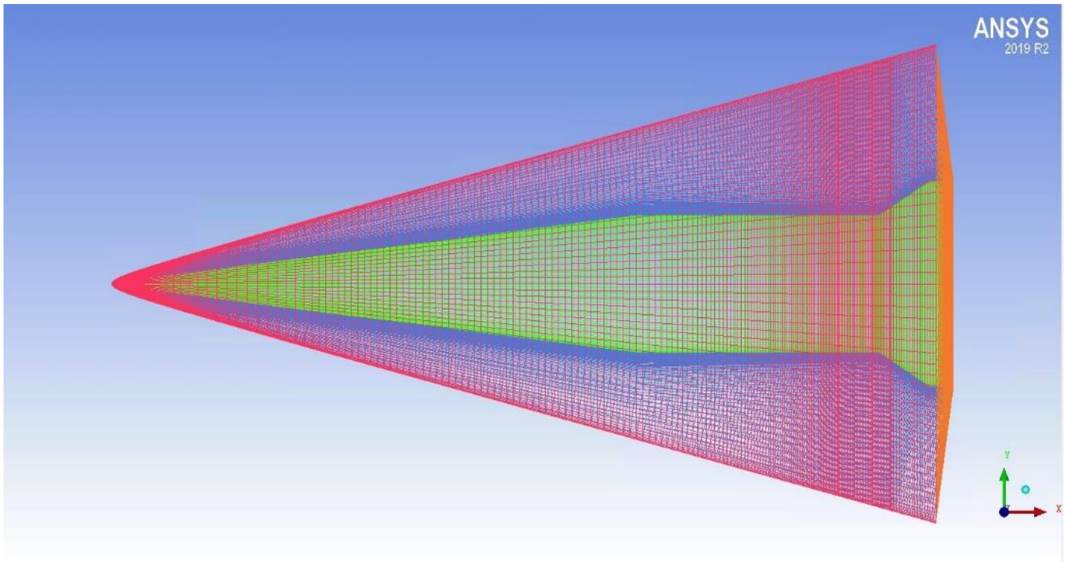

Figure 3.3 3D cross-section grid on the surface and around the full HIFiRE-1 geometry.

Similar meshes were provided and imported into ICEM for the finer mesh sizes. The full geometry meshes consisted of coarse (3L), medium (2L), and fine (1L) grid refinements. Note that the distinction of the numbers (from 3 to 1), followed by “L,” are the dictated abbreviations provided with the cgns files for the mesh. Table 3.1 displays some of the important mesh information for each of the three full geometry meshes.

Table 3.1 HIFiRE-1 full geometry mesh information and elemental breakdown.

		Coarse (3L)	Medium (2L)	Fine (1L)
Element Parts	Flow Domain	2,031,616	16,252,928	130,023,424
	Inlet	15,872	63,488	253,952
	Outlet	8,192	32,768	131,072
	Symmetry	65,536	262,144	1,048,576
	Wall	15,872	63,488	253,952
Summary	Total Elements	2,137,088	16,674,816	131,710,976
	Total Nodes	2,084,769	16,464,705	130,868,865

3.3 Numerical Method and Boundary Conditions

A density-based solver in ANSYS Fluent was used for all CFD simulations along with the energy equation. The two cases studied have a free stream Mach number of 7.18 at an operating pressure of 0 Pascals with two different angles of attack of 0° and 2°.

According to the 2022 High-Fidelity CFD Workshop, boundary conditions are to be set based on the type of the solver [2]. The inlet boundary condition was set as a velocity inlet with the following component velocities accounting for α = 2°: V_x = 2580.667 m/s and V_y = 90.119 m/s. For α = 0° the velocity components were set as: V_x = 2582.257 m/s and V_y = 0 m/s. The wall was set as an isothermal non-slip wall with T_w = 411.7229 K based on the wall temperature ratio of $\frac{T_w}{T_\infty}$ = 1.279 and T_∞ = 321.91 K. The outlet boundary condition was set as a pressure outlet at P_{outlet} = 6480 Pa.

The spatial discretization of the solver had the following settings at start of the simulation: Green-Gauss node-based gradient, first- order-upwind scheme for the flow, and first-order upwind scheme for the modified turbulent viscosity. The solution utilized implicit formulation with a Roe-FDS flux-type. The numerical methods were further controlled with a 0.25 relaxation factor and a 0.5 Courant number. After a sufficient time throughout the solution process, the schemes for flow and modified turbulent viscosity were both switched to second order upwind. The turbulence model utilized in the simulations is described below:

3.3.1 Spalart-Allmaras (SA) Turbulence Model

A widely utilized turbulence model for many aerodynamic flows is the one-equation Spalart-Allmaras (SA) turbulence model. This turbulence model utilizes a single transport equation for the turbulent eddy viscosity. This model can be utilized for shock-induced separation, which is important for the HIFiRE-1 computational simulations since shock-induced separation is expected to occur. The SA model can also be used for the following conditions for compressible flow with heat transfer: A perfect gas assumption with Pr = 0.72, Pr_t = 0.90, and Sutherland's law for dynamic viscosity [5]. For this analysis, the fluid is air with modified parameters based on the previously mentioned conditions set forth for the SA model since the HIFiRE-1 flow-field is hypersonic, and hence compressible with heat transfer. It has been shown that the SA model can accurately predict shock-induced separation and responds to steep pressure gradients; however, there are difficulties in the ability of the model to compute post-shock reattachment in adverse pressure gradients [6]. The one-equation SA model is given by Eq. (3.1) in the non-conservation form as [5]:

$$\frac{\partial \hat{\nu}}{\partial t} + u_j \frac{\partial \hat{\nu}}{\partial x_j} = c_{b1}(1 - f_{t2})\hat{S}\hat{\nu} - \left[c_{w1} f_w - \frac{c_{b1}}{\kappa^2} f_{t2}\right]\left(\frac{\hat{\nu}}{d}\right)^2 + \frac{1}{\sigma}\left[\frac{\partial}{\partial x_j}\left((\nu + \hat{\nu})\frac{\partial \hat{\nu}}{\partial x_j}\right) + c_{b2}\frac{\partial \hat{\nu}}{\partial x_j}\frac{\partial \hat{\nu}}{\partial x_j}\right] \quad (3.1)$$

where $\hat{\nu}$ denotes the turbulent kinematic viscosity. The details of the SA model can be found in Refs. [5] and [6].

3.4 Results

3.4.1 Analysis of Flow over HIFiRE-1 Full Geometry at M = 7.18 and α = 2°

Computational analysis was conducted in ANSYS Fluent for the HIFiRE-1 full geometry at α = 2° and 0° with M = 7.18 using an energy equation enabled density-based solver employing the Reynolds-Averaged Navier-Stokes (RANS) equations with the SA one-equation turbulence model. For a baseline computational comparison, the results from the 2022 High-Fidelity CFD workshop are utilized to compare the present computations in numerical values and overall trends with those of participants in the workshop. The workshop results consist of computational results from various organizations using different codes [7].

Pressure Distribution

In Figure 3.4, comparisons are made between the present computational analysis and the computational results from the workshop for the non-dimensionalized pressure (obtained dividing by P_∞). Figure 3.4 summarizes the normalized pressure results on leeward side, windward side, and in symmetry plane of HIFiRE-1 at 2° angle of attack on multiple meshes from MetaComp, Langley Research Center (LaRC), and Sandia National Lab. (SNL) [7]. In Fig. 3.4, the leeward pressure corresponds to the normalized pressure on surface of the wall along the intersection of the wall and the symmetry plane on the lee side of the incoming freestream at 2° angle of attack, the windward pressure runs along the intersection of the wall and the symmetry plane on the windward side of the incoming freestream at 2° angle of attack, and the symmetry plane pressure correlates to the pressure along the intersection of the wall and the x-z plane (i.e. the location where the flow is symmetric on either side of the geometry).

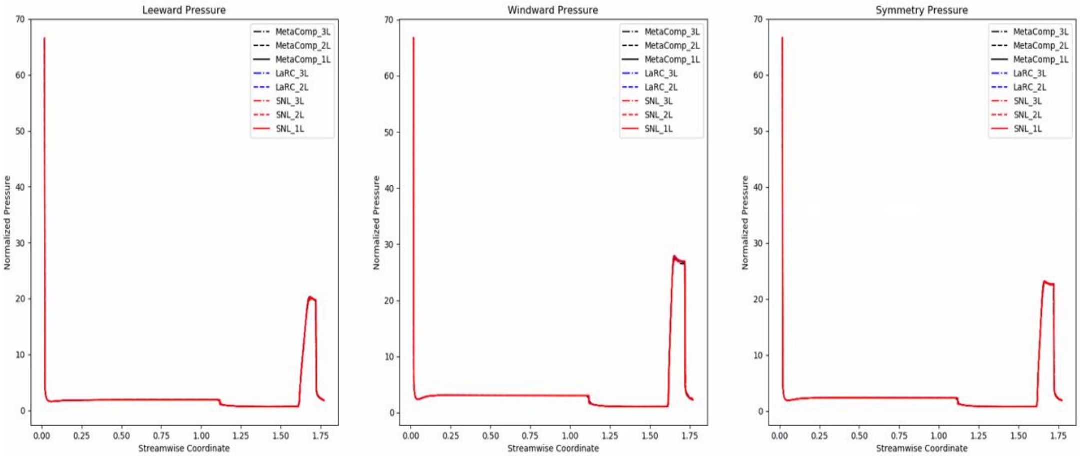

Figure 3.4 Computed non-dimensionalized pressure on leeward side, windward side and in symmetry plane of HIFiRE-1 at 2° angle of attack performed by three different organizations (MetaComp, LaRC and SNL) on multiple meshes [7].

The results of present computations for the non-dimensionalized pressure on leeward side, windward side and symmetry plane of HIFiRE-1 are shown in Fig. 3.5. The overall non-dimensionalized pressure profiles between the workshop results (Fig. 3.4) and the present computational simulation results (Fig. 3.5) have a similar profile and are of similar magnitudes. It should be noted that in Fig. 3.5, computations are shown on each of the three provided meshes and they are nearly identical.

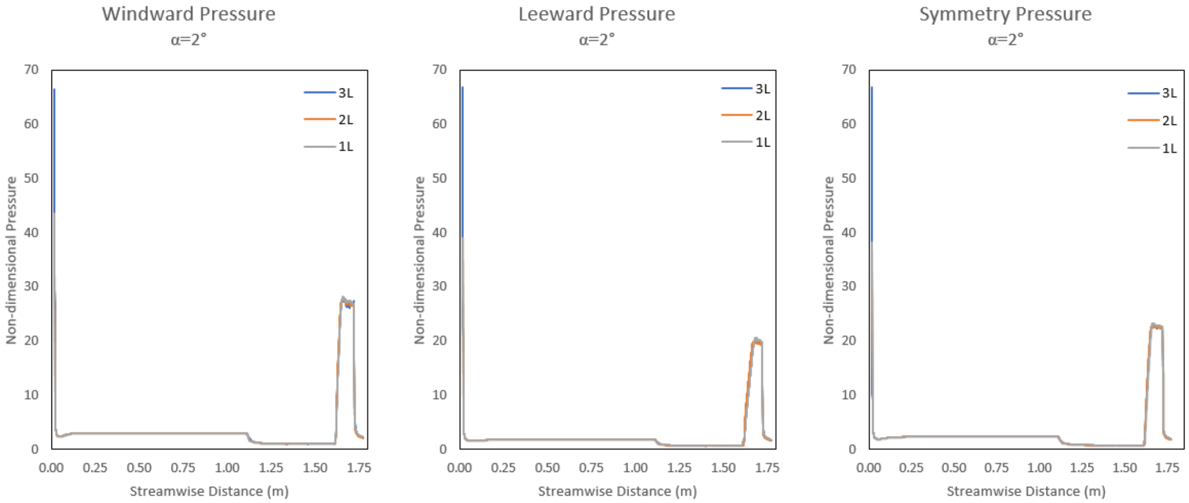

Figure 3.5 Present computations of non-dimensionalized pressure on leeward side, windward side and in symmetry plane of HIFiRE-1 at 2° angle of attack.

To further compare the present computed solutions at $\alpha = 2°$, we zoom into specific locations on the geometry and compare our normalized pressure results from the workshop participant results from MetaComp, LaRC and SNL. Figure 3.6 shows the pressure profiles obtained from the three workshop participants for the flare section of the HIFiRE-1 full geometry (from 1.5 m to 1.77 m). It should be noted that the non-dimensionalized static pressure is clearly much higher on the windward side than on the leeward side as expected. The overall pressure profile also corresponds to an increase in pressure as the geometry transitions into the flare section, and as the flare levels out at the end of the geometry the pressure profiles show a sharp decrease in pressure. Similar features in the pressure profiles are in the present results shown in Fig. 3.7 and are of similar magnitude.

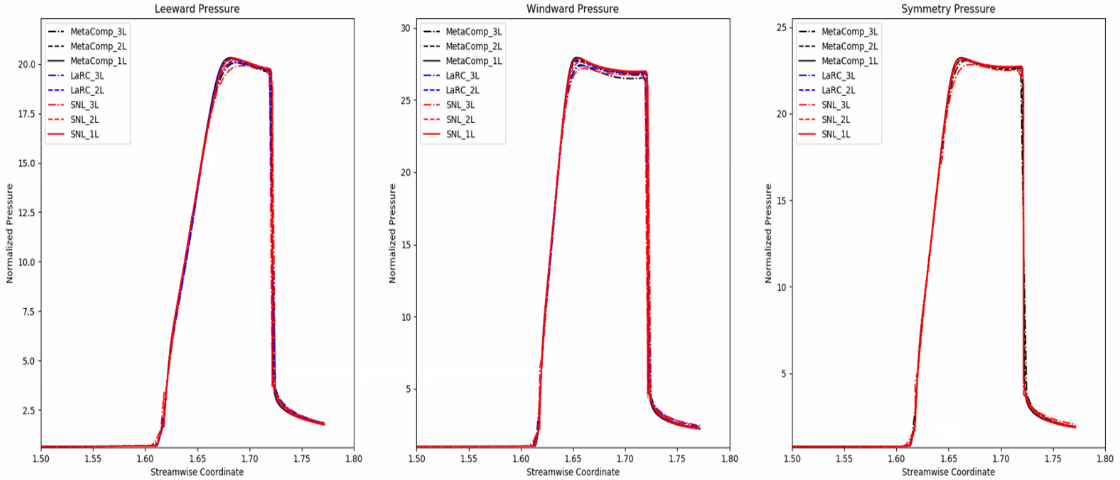

Figure 3.6 Zoomed-in non-dimensionalized pressure profiles in the flare region obtained by MetaComp, LaRC and SNL.

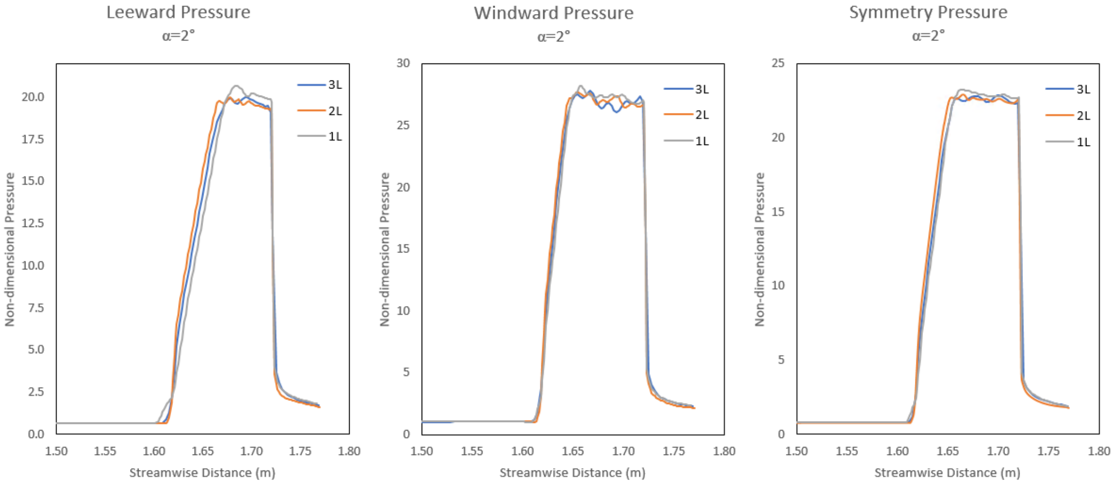

Figure 3.7 Present results for the zoomed-in non-dimensionalized pressure profiles in the flare region on all three meshes.

It can be noted from Fig. 3.6 and Fig. 3.7 that the shape and magnitude of the normalized pressure profiles are consistent in present computations with those of the workshop participants in the 2022 High-Fidelity CFD workshop. In Fig. 3.7, there is some notable instability in peak portion of these pressure profiles; it is likely due to the sharp increase in pressure at this section causing the numerical scheme to become slightly unstable for the number of iterations employed in obtaining the computed solution. This problem would be rectified if the solution is carried out to a larger number of iterations along with further mesh refinement in that area. It is seen from present computations on the finest mesh (1L) that most of the instability at the flare peak is resolved due to the refined mesh.

Heat Flux Distribution

The most important quantity of interest in any hypersonic flow simulation is the heat flux along the wall of the geometry. The heat flux is of great importance due to the large buildup of heat on the wall of a structure in a hypersonic freestream. Along with the non-dimensionalized pressure profiles given above, non-dimensionalized heat flux profiles were computed. The heat flux results were non-dimensionalized by $\frac{\kappa_\infty T_\infty}{r}$, where r is the radius of the cylindrical section of the HIFiRE-1 geometry. Figure 3.8 shows the computed non-dimensionalized heat flux profiles on the leeward side, windward side, and symmetry plane of HiFIRE-1 on each of the three provided meshes. The solutions for these three meshes are close to each other except for some minor differences in the peak heat flux region.

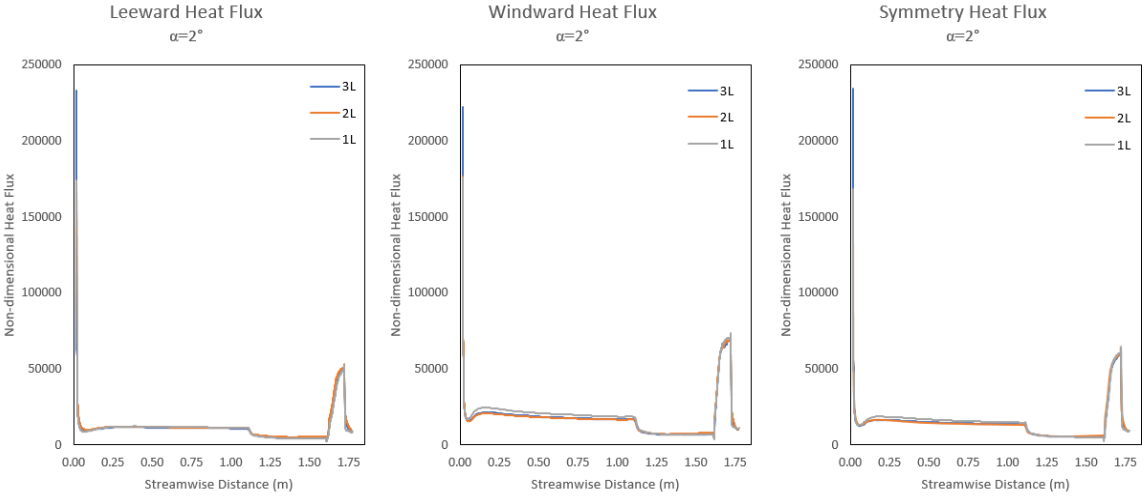

Figure 3.8 Present computations of non-dimensionalized wall heat flux along leeward side, windward side, and symmetry plane on each of the three meshes.

The overall variation and trend in the heat flux profiles is similar to that of the pressure profiles, but there are key differences especially near the flare section of the geometry where the heat flux is largest (not considering the stagnation region at the front tip of the geometry). The flare region, starting at ~1.6 m and extending to nearly the end of the geometry, has a steep but gradual increase in the heat flux until the flare section levels off. At that point the heat flux is at its largest peak value and then has a rapid decrease until the end of the geometry.

Figure 3.9 shows the zoomed-in profiles of the computed normalized heat flux in flare region. Figure 3.10 shows the zoomed-in profiles of the normalized heat flux that were obtained from the 2022 High-Fidelity CFD Workshop. These profiles have the same trend as well as magnitudes within 5% as Fig. 3.9 leading to further affirmation that the present simulation results are consistent with the workshop results from three different investigators. Again, there is some instability that shows some waviness in the upper part of the profiles, but the overall results are consistent in shape and magnitude with the results of other participants from the workshop. Another important takeaway from these results is that as the mesh is refined from 3L to 1L, the curve is slightly less smooth, but all the important flow features are captured by each mesh.

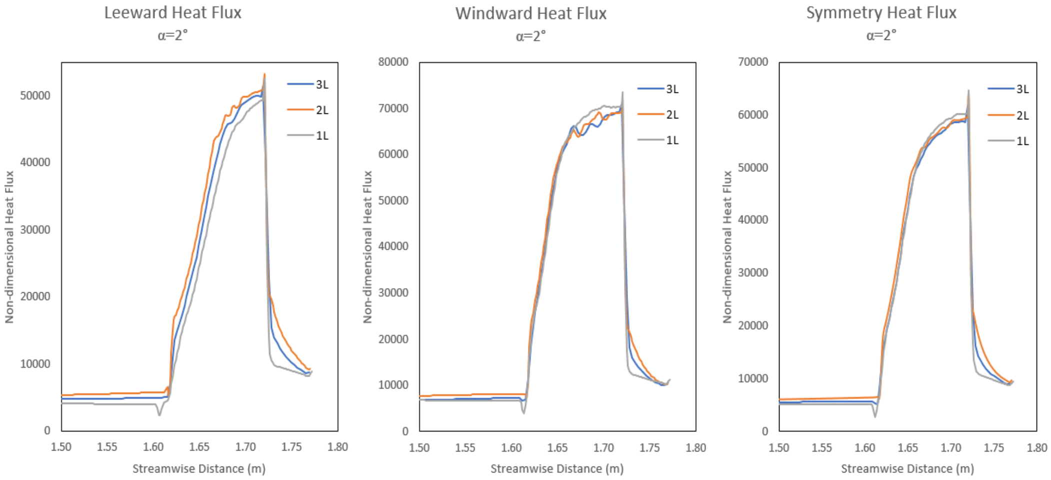

Figure 3.9 Present computed results for zoomed-in non-dimensionalized wall heat flux at the flare section on each of the three provided meshes.

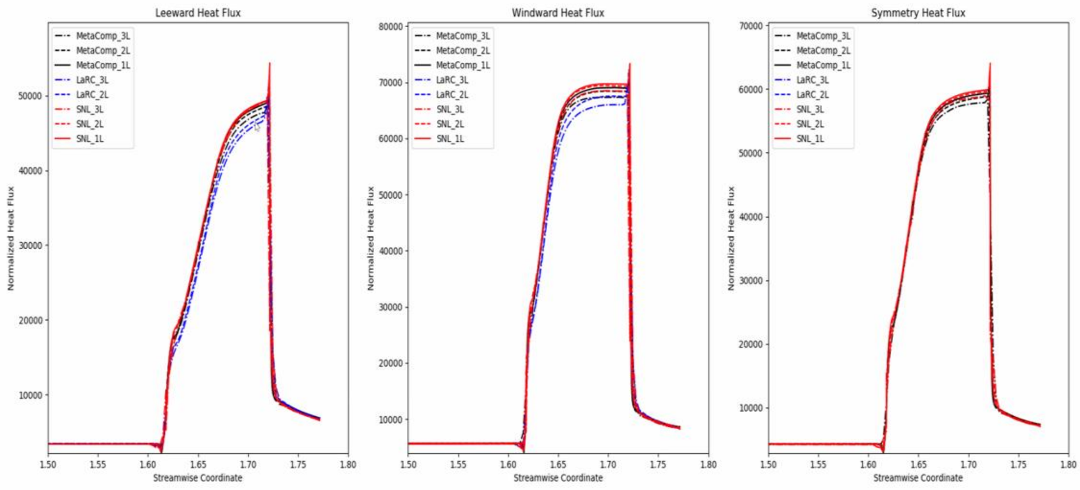

Figure 3.10 Zoomed-in non-dimensionalized wall heat flux at the flare section obtained from three workshop participants (MetaComp, LaRC and SNL) on various meshes.

Skin-Friction Distribution

In addition to heat flux, another quantity of interest is the skin-friction C_f along the surface of the body. The workshop did not focus on the profiles of C_f, but this is an important quantity in hypersonic flow since it relates to surface shear stress within the boundary layer in various flow regimes of the hypersonic body. This is particularly important since it also correlates with the overall heat transfer to the wall. Figure 3.11 displays the computed skin friction coefficient profiles along the leeward side, windward side, and the line of flow symmetry. The C_f profiles follow the same general trend as the heat flux profiles, but the peak is much more prominent near the flare section where there is also largest change in heat flux. At the onset of the flare there is a steep drop in the C_f values and after the decrease, there is the rapid and smooth increase as seen in the heat flux profiles (Figs. 3.9 and 3.10).

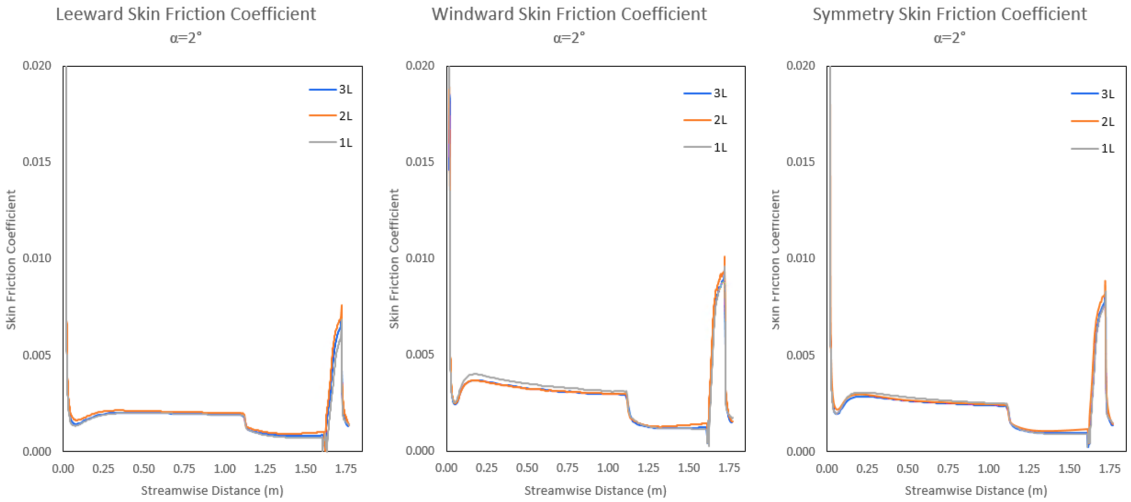

Figure 3.11 Computational results for the skin friction coefficient on all three provided meshes.

Apart from the very small instabilities in the profiles of non-dimensionalized pressure and heat flux, the present computed results overall are within 5% of the results obtained from the 2022 High-Fidelity CFD workshop. This shows that the present simulations are consistent and compare well in accuracy with the results of other workshop participants for HIFiRE-1 for the same flow conditions of $M = 7.18$ and $\alpha = 2°$ [2].

3.4.2 Analysis of Flow over HIFiRE-1 Full Geometry at M = 7.18 and α = 0°

Further analysis of the HIFiRE-1 problem was conducted for $\alpha = 0°$ under the same boundary conditions and flow properties. This case was not computed by the 2022 Hi-Fidelity CFD Workshop participants. The 0° angle of attack case is computationally simpler since the entire geometry is axisymmetric and the flow is also axisymmetric; therefore, there is no windward or leeward side on the geometry. Due to computational limitations the finest mesh for this flow condition was not studied. Figure 3.12 shows the computed results for the non-dimensionalized pressure and heat flux profiles along an intersection of the wall and the x-z plane.

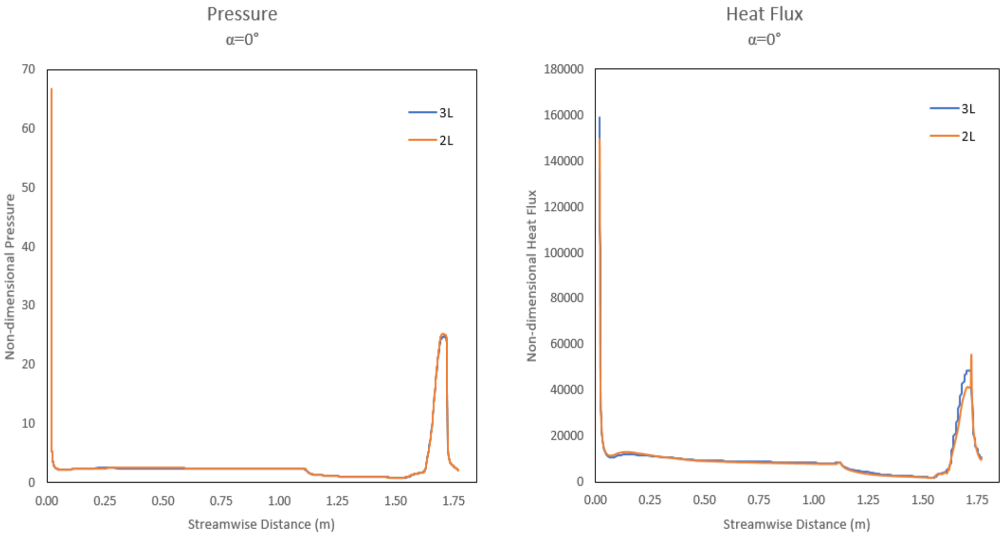

Figure 3.12 Computed results for non-dimensionalized pressure and heat flux at $\alpha = 0°$.

The overall trends in Fig. 3.12 for pressure and heat flux remain consistent with those in the $\alpha = 2°$ simulations with the values being similar in the x-z flow symmetry plane (Figs. 3.5 & 3.8). The non-dimensional pressure profiles correlate well with one another between the 3L and

2L mesh, but a clear discrepancy is seen in the non-dimensional heat flux profile in Fig. 3.12. The 3L mesh results produce a much broader peak in heat flux at the flare section at ~1.6 m, whereas for the 2L mesh the results have a much narrower peak with a large spike in heat flux near the end of the flare. This trend is likely due to convergence issues on the coarser mesh, or an issue with mesh refinement in that interest area where there are complex flow features occurring, resulting in this heat flux profile discrepancy. As with the 2° angle of attack case, the pressure results can be zoomed-in on the flare region to further investigate the inconsistencies between the results for both meshes. Figure 3.13 below shows the comparison between the pressure profiles at the flare section using 3L and 2L mesh.

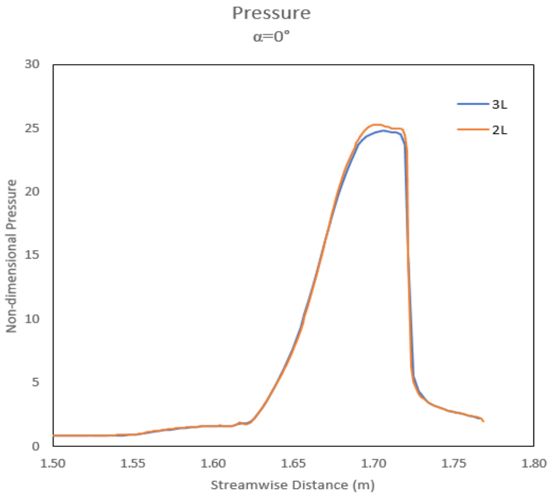

Figure 3.13 Computed results for pressure at $\alpha = 0°$ on the coarse (3L) and medium mesh (2L).

These pressure profiles correlate well with one another throughout the whole profile, except for a slight discrepancy at the peak pressure in the flare region (Fig. 3.13). Flare focused profiles are also generated for the heat flux results as shown in Fig. 3.14 below.

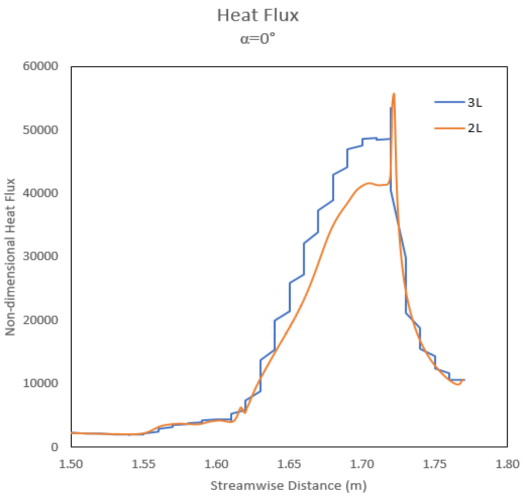

Figure 3.14 Computed results for heat flux at α = 0° on the coarse (3L) and medium mesh (2L).

For this 0° angle of attack case the medium (2L) mesh provides much smoother and more expected results for the heat flux in the flare region. The coarse (3L) mesh results follow a similar trend in this flare section as the medium mesh, however the results are rough and jagged, likely due to mesh refinement in this area. The smooth behavior of the medium mesh heat flux profile models a trend that is more expected for this symmetric simulation case and the coarse mesh results offer only a rough estimate of the expected trend. As with the 2° case, skin friction profile results are presented for the overall geometry (Fig. 3.15).

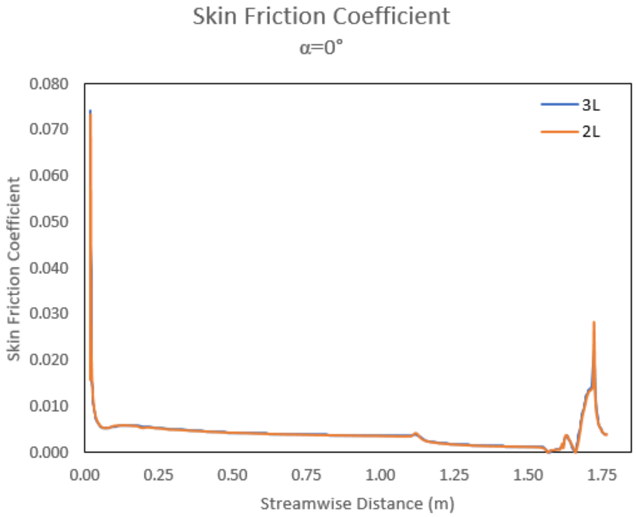

Figure 3.15 Skin friction coefficient results at α = 0° on the coarse (3L) and medium mesh (2L).

From these skin friction profiles, it is evident that the numerical instability in the heat flux results from the coarsest mesh is not as evident in the skin friction profiles for the coarse mesh. Further information about the 0° angle of attack case can be obtained by observing the Mach contours on the XY-symmetry plane. Mach contours were calculated using Eq. (3.2) with $\gamma = 1.4$, R for air = 287 $\frac{J}{kg*K}$, and utilizing the calculated temperature and velocity fields for the given flow field. The computed Mach contours utilizing the computational results for the coarse mesh (3L) are shown in Fig. 3.16.

$$M = \frac{V}{\sqrt{\gamma R T}} \tag{3.2}$$

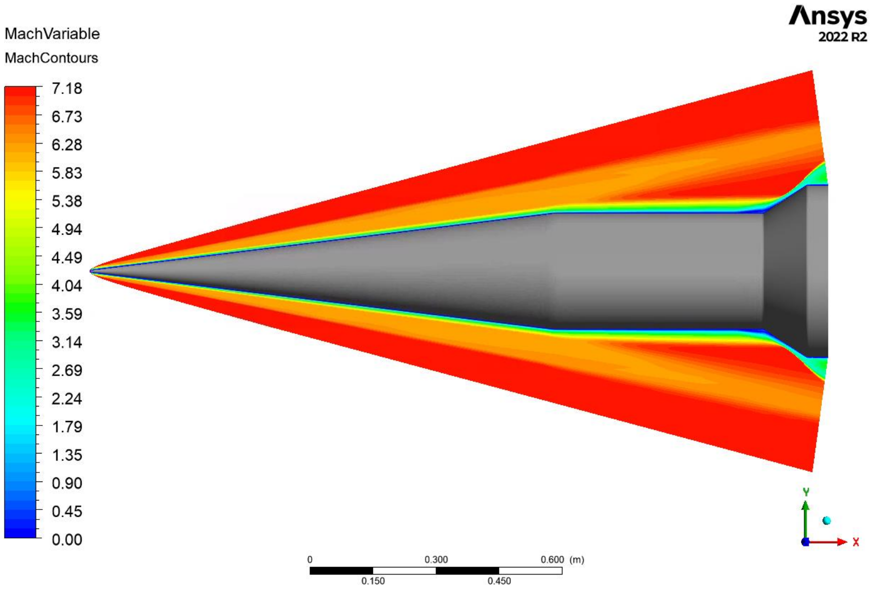

Figure 3.16 Mach contours on the x-y symmetry plane at α = 0° for the 3L mesh.

From the Mach contours on the symmetry plane, it is clear to see important hypersonic compressible flow features. Some key features are the expansion of the flow at the location where the cone meets the long flat cylindrical section. This expansion causes an expansion fan to propagate outward and along the surface of the geometry thereby increasing the Mach number in this location. Near the flare section there is a dramatic reduction in the Mach number of the external flow field leading to the conclusion that a turbulent separation zone is present in the flow field due to an oblique shock wave generated by the sharp turning angle caused by the flare. Another key characteristic shown by the Mach contours is the detached bow shock wave in front of the HIFiRE-1 geometry and extending around the object. The present simulation results are similar to the experimental and computational results from the HIFiRE-1 transition experiment at $M = 7.16$ and $\alpha = 0°$ [1]. The experimental and computational analyses results in Fig. 3.17 depict the overall flow field characteristics with labels for relevant features of the flow field with over-laid calculated Mach contours.

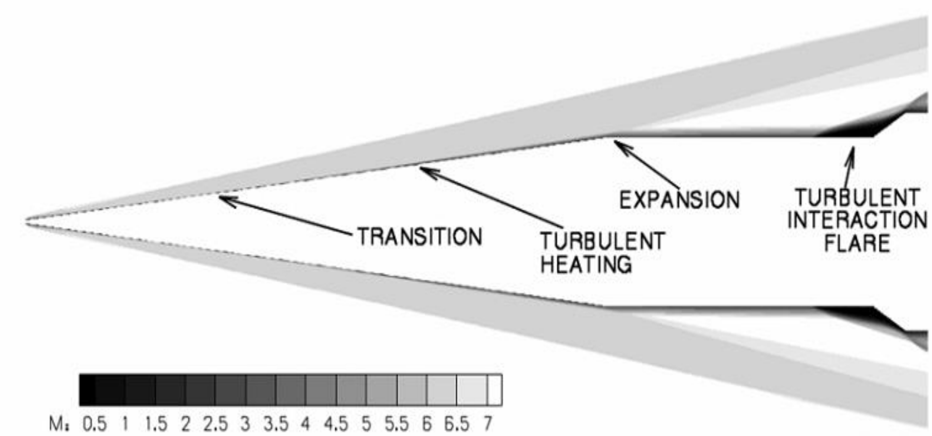

Figure 3.17 Experimentally calculated Mach contours with labelled flow features of interest [3].

Due to the nature of this present computational study, the transition region was not computed since a transitional model was not part of the topic of interest. It is also important to note that the experimental results shown in Fig. 3.17 focus on a similar case as the present computational case, but there are differences in the simulation model as well as the experiment and therefore the present results should not be directly compared with results from the ground test studies for the 0° angle of attack case. Figure 3.17 is included here for qualitative description of some of the flow features especially in the corner region of the flare. Furthermore, experimental data contains transitional flow data that has not been simulated in the present computational case since the SA one-equation turbulence model does not calculate transitional flow; it assumes a fully turbulent flow. The experimental results show laminar to turbulent transition in the boundary layer on the conical section of the HIFiRE-1 geometry.

3.5 Conclusions

CFD simulations for the HIFiRE-1 geometry have been conducted using the Reynold-Averaged Navier-Stokes (RANS) equations with one-equation Spalart-Allmaras (SA) turbulence model in ANSYS Fluent to simulate the hypersonic flow field at Mach 7.18 and an angle of attack $\alpha = 0°$ and 2°. The simulations show that the present numerical results are accurate when comparing the results for non-dimensionalized pressure and heat flux profiles with those reported in the 2022 High-Fidelity CFD Workshop for the $\alpha = 2°$ case. The computational results are within 5% of the results reported in the workshop by other investigators from MetaComp, NASA Langley Research Center and Sandia National Lab. The results follow the same general trend for each of the three provided meshes. Numerical results for the skin-friction, C_f, profiles are also provided as they serve to provide necessary information about the wall surface shear stress within the boundary layer. Skin-friction profiles have not been reported by the workshop; they can be helpful to other investigators interested in computing this flow. In addition, computations and analysis are also presented for $\alpha = 0°$ case, which has not been computed by High Fidelity CFD workshop participants. The analysis of the $\alpha = 0°$ case gives acceptable values on both the coarse and medium meshes with trends that follow those of the $\alpha = 2°$ case on the x-y flow symmetry plane. The coarse and medium meshes provide acceptable results for non-dimensionalized pressure, however there is a clear sharpness in the heat flux profile for the coarse mesh. The general trend depicted by the medium mesh results is modeled by the coarse mesh but with a jagged curve that does not offer a smooth trend. Through analysis of the Mach contours, the computations clearly show an expansion region near the end of the cone section of the geometry, which is consistent with the experimental flow features. Additional computational analysis is required for $\alpha = 0°$ case since the unmodified SA one-equation turbulence model does not predict transitional flow that is seen in the experimental test studies.

3.6 References

[1] Wadhams, T. P., Mundy, E., MacLean, M. G., and Holden, M. S., "Ground Test Studies of the HIFiRE-1 Transition Experiment Part 1: Experimental Results," Journal of Spacecraft and Rockets, Vol. 45, No. 6, 2008, pp. 1134–1148. https://doi.org/10.2514/1.38338.

[2] Fisher, T., "High Fidelity CFD Workshop 2021: High Speed Steady Challenge Case: Hi-Fire 1," NASA Langley Research Center Turbulence Modeling Resource, 2021. URL: https://turbmodels.larc.nasa.gov/Highfidelitycfd2021/SteadySupHypersonic_hifire_HFW_2021.pdf.

[3] MacLean, M., Wadhams, T., Holden, M., and Johnson, H., "Ground Test Studies of the HIFiRE-1 Transition Experiment Part 2: Computational Analysis," Journal of Spacecraft and Rockets, Vol. 45, No. 6, 2008, pp. 1149–1164. https://doi.org/10.2514/1.37693.

[4] "Index of /HFW2022/HiFire1/Pointwise," Massachusetts Institute of Technology Aerospace Computational Design Laboratory, 2021, Cambridge, MA. URL: https://acdl.mit.edu/HFW2022/HiFire1/Pointwise/.

[5] Rumsey, C., "The Spalart-Allmaras Turbulence Model," NASA Langley Research Center Turbulence Modeling Resource, 2022. UR: https://turbmodels.larc.nasa.gov/spalart.html#sa.

[6] Spalart, P. R., and Allmaras, S. R., "A One-Equation Turbulence Model for Aerodynamic Flows," AIAA Conference Paper AIAA-92-0439, 30th Aerospace Sciences Meeting and Exhibit, Reno, NV, 1992. https://doi.org/10.2514/6.1992-439.

[7] Rumsey, C., and Wukie, N., "High Fidelity CFD Workshop 2022," NASA Langley Research Center Turbulence Modeling Resource, 2022. URL: https://turbmodels.larc.nasa.gov/highfidelitycfd_workshop2022.html.

Chapter 4: Laminar Steady Hypersonic Flow past Blottner Sphere

4.1 Introduction

The laminar hypersonic flow past a Blottner Sphere has been investigated by many researchers theoretically and experimentally since the early 1960's and more recently computationally. Early solutions to the hypersonic flow past this sphere utilized numerical methods to solve the Navier-Stokes equations that govern the flow field with a constant density approximation [1]. Over the years, the Blottner Sphere problem has been adopted as a benchmark test case for hypersonic laminar flow over a spherical body, which has been used for verification of CFD codes [2]. Since this test case has shown importance in the development, verification, and validation of CFD solvers, it was chosen as one of the test cases for the 2022 High-Fidelity CFD Workshop by NASA Langley Research Center in association with AIAA. This test case was chosen by the workshop with the purpose of "evaluating the ability of solvers to correctly and efficiently predict heating on the surface of a sphere in a three-dimensional high-speed flow," using a provided set of meshes. The governing equations for this test case are the three-dimensional compressible Navier Stokes equations with the perfect gas assumption and Sutherland's Law of viscosity [3]. This test case involves steady high-speed flow at Mach 5.0 for the Blottner sphere, which is not a full sphere but rather a hemisphere with a 0.127 m diameter. The diameter of the sphere in the High-Fidelity CFD workshop case ($d = 0.127\ m$) [3] differs from the reference diameter used in the original Blottner Sphere study ($d = 0.027\ m$) [2]. Figure 4.1 shows the hemispherical geometry of the Blottner Sphere.

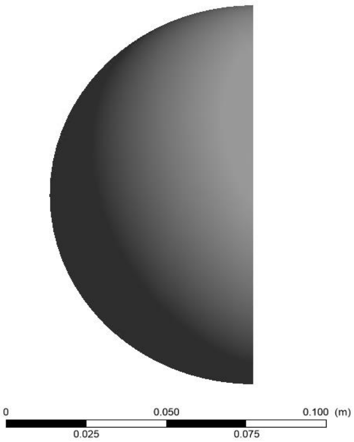

Figure 4.1 Hemispherical geometry of the Blottner Sphere.

The computation of the hypersonic flow field of Blottner Sphere for verification and validation of a CFD solver is of great interest since there are many studies already published with computational data involving this case. There are also several experimental results containing data for the Blottner Sphere as part of the experiments on leading nose tip in many studies. One such study has results for transitional and turbulent heat transfer measurements over a conical nose tip, where the leading nose tip is of the same geometry and the flow parameters are similar to that in the Blottner Sphere case [4]. This section aims to further investigate the Blottner Sphere test case for verification and validation of steady hypersonic computational analysis methods in ANSYS Fluent for application in future hypersonic flow cases. The 2022 High-Fidelity CFD Workshop included results from four separate contributors: MetaComp Technologies, NASA Langley Research Center, University of Strasbourg in France, and Sandia National Laboratories.

4.2 Computational Mesh

The High-Fidelity CFD Workshop provided several meshes including structured, unstructured, and higher order curved meshes [5]. The meshes were provided with .cgns files that were loaded into ANSYS ICEM CFD 2022 R2 and then exported to ANSYS Fluent for flow field analysis. The meshes contained an inlet, outlet, wall, and flow domain elemental parts. Figure 4.2 shows the provided medium mesh where the leading hemisphere wall is depicted with blue elements, and the inlet is shown with purple elements, and the outlet is shown in green in the frontal view of the mesh.

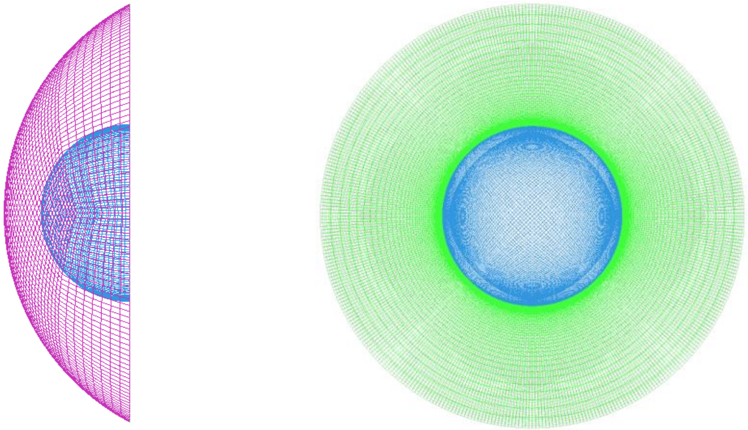

a) Side View b) Rear View

Figure 4.2 Computational mesh (Medium provided mesh) with elements shown for wall (blue), inlet (purple), and outlet (green).

Meshes were provided on the sizing scale of Wee to Fine, with Wee being the coarsest mesh and Fine being the most refined mesh [5]. The inlet, outlet, and wall elements were meshed utilizing the four node quadrilateral elements, and the internal flow domain was meshed with eight node hexahedral elements. Table 4.1 below summarizes the mesh information for all five of the provided meshes.

Table 4.1 Blottner sphere mesh information and elemental breakdown.

		Wee	Tiny	Coarse	Medium	Fine
Element Parts	Flow Domain	3,840	30,720	245,760	1,966,080	15,728,640
	Inlet	240	960	3,840	15,360	61,440
	Outlet	768	3,072	12,288	49,152	196,608
	Wall	240	960	3,840	15,360	61,440
Summary	Total Elements	5,088	35,712	265,728	2,045,952	16,048,128
	Total Nodes	4,505	33,297	255,905	2,006,337	15,889,025

4.3 Numerical Methods and Boundary Conditions

The Blottner Sphere problem was simulated matching the flow conditions outlined by Blottner [2] and the High-Fidelity CFD Workshop [3]. ANSYS Fluent was employed with the steady density-based solver and the laminar flow model built into Fluent with the Energy Equation turned on. The air was set to have the density based on the perfect gas law with a constant specific heat ($C_{p_\infty} = 1004.652\ \frac{J}{kg*K}$), a constant thermal conductivity ($\kappa_\infty = 0.00719135\ \frac{W}{m*K}$), constant molecular weight ($M_{air} = 28.966\ \frac{kg}{kmol}$), and the Three-Coefficient Method of Sutherland’s Law of Viscosity to determine the dynamic viscosity of air. Equation 4.1 describes the Sutherland’s law of viscosity using the Three-Coefficient Method:

$$\mu = \mu_{ref}\left(\frac{T}{T_{ref}}\right)^{3/2}\frac{T_{ref}+S}{T+S} \tag{4.1}$$

where $\mu_{ref} = 1.716 \times 10^{-5}$ is the reference viscosity at the reference temperature $T_{ref} = 273.15\ K$ and S is the Sutherland temperature, $S = 110.4\ K$ [6].

The inlet is defined as a pressure far field with freestream conditions for temperature $T_\infty = 75.661\ K$, a gauge pressure of $P_\infty =$ 1907.4051 Pa, a Mach number $M = 5.0$, and the flow direction set to be solely in the x-direction (i.e., $\alpha = 0°$). The outlet is a pressure outlet defined with the same gauge pressure and temperature as the inlet. The wall of the sphere is a no slip, isothermal wall with a wall temperature ratio of $\frac{T_w}{T_\infty} = 1.308$, which defines the wall temperature $T_w = 98.889\ K$. Other important parameters used to set the boundary conditions are as follows: $\gamma = 1.4$, $Pr = 0.72$, $Re_D = 1.8875\ \times 10^6$, $V_\infty = 871.5667\ m/s,$ and $\rho_\infty = 0.087884\ kg/m^3$.

The solution method used is the implicit formulation and the Roe-FDS flux type scheme with the spatial discretization gradient set to Green-Gauss Cell based method with a First-Order Upwind flow scheme. After an appropriate amount of convergence has occurred in the solution, the flow scheme is switched to the Second-Order Upwind scheme. To further control the solution process, the Courant Number in Fluent is set to 0.5 and is varied to a maximum value of 4 in the solution process as feasible.

4.4 Results

Using the numerical method and boundary conditions described in the sections above, computational simulations were conducted utilizing the Washington University in St. Louis' engineering computing cluster with ANSYS Fluent 21 using batch job submission. Simulations were completed for all five meshes. Computational results are compared to the results obtained by each of the four contributors to the High-Fidelity CFD Workshop focusing on normalized values of surface pressure and surface heat flux. Before comparing results to those of the workshop participants, Mach contours for both the Wee and Medium meshes are plotted in the

XY Plane to analyze the development of the bow shock in front of the sphere as well as how the flow behaves as it hits the wall (Figure 4.3).

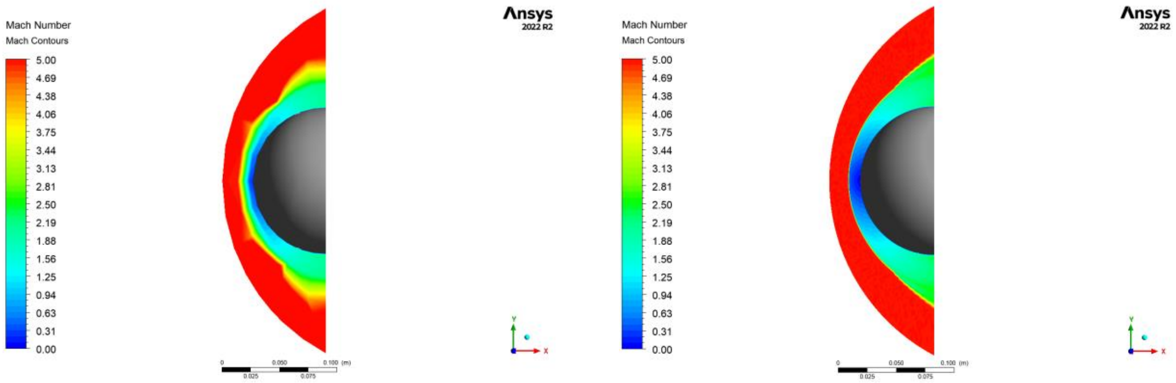

a) Wee Mesh

b) Medium Mesh

Figure 4.3 Mach contours on the XY Plane.

The Mach contours and the wall (shown in gray) shown in Fig. 4. 3 depict the Mach 5.0 freestream condition persisting until the bow shock is at approximately 0.0095 m in front of the stagnation point of the sphere. Similar contour plots are obtained for all other meshes but the purpose of contour plots for the two meshes shown in Fig. 4.3 is to depict the differences in the the shock development due to the density of the grid. Since the flow domain in the case of coarser mesh has much less refinement compared to the finer mesh, therefore the shock is captured much better as well several other flow features with more accuracy in case of finer mesh as expected.

Further analysis of the results is completed by obtaining the profiles for surface values taken along the intersection of the wall and XY-Plane as shown by the green curve in Fig. 4.4 which intersects the wall (shown in blue). Results are obtained along this line and the plotted distance is determined by the distance from the central axis of the sphere along the intersection line.

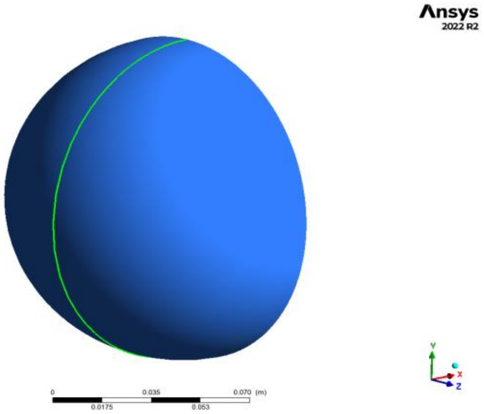

Figure 4.4 Data location line along the intersection of the wall and YZ-plane

The results obtained by the four workshop participants had a small spread in the normalized surface pressure of approximately 0.5 and a very large spread of approximately 200 in the normalized surface heat flux. The surface pressure is normalized with respect to the freestream pressure ($P_\infty = 1907.4051$ Pa) and the surface heat flux is normalized with respect to the freestream thermal conductivity, freestream temperature, and half of the radius of the sphere by the expression ($\frac{\kappa_\infty\, T_\infty}{d/4}$). Half of the radius of the sphere was chosen as the normalization factor to maintain consistency with the results produced by the workshop participants. Out of all four participants in the workshop, MetaComp Technologies was the only participant that reported results for all five of the provided (structured) meshes that have also been considered in this thesis along with some unstructured meshes whose results are not reported in this thesis. Surface pressure profiles for all five meshes are shown in Fig. 4.5 along with the workshop results from one of the contributors. There is a clear difference in the results for the coarser meshes, but as the mesh becomes finer, the present surface pressure profiles become closer to that of the workshop participants. The present surface pressure profiles are not more than 5% different from the other workshop participants’ results for the coarse, medium, and fine meshes.

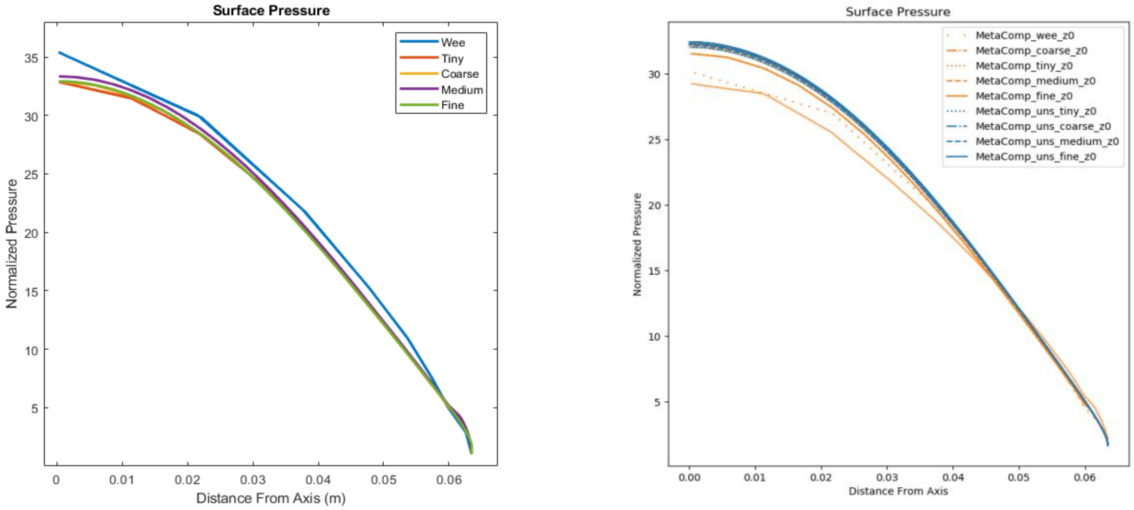

a) Present results b) Workshop participant results (MetaComp Tech.)

Figure 4.5 Normalized surface pressure profiles.

Normalized heat flux profiles on the surface of Blottner Sphere were also obtained for all of the meshes except for the finest provided mesh. Figure 4.6 summarizes the present surface heat flux results for four out of the five meshes as well as results from one of the workshop participants.

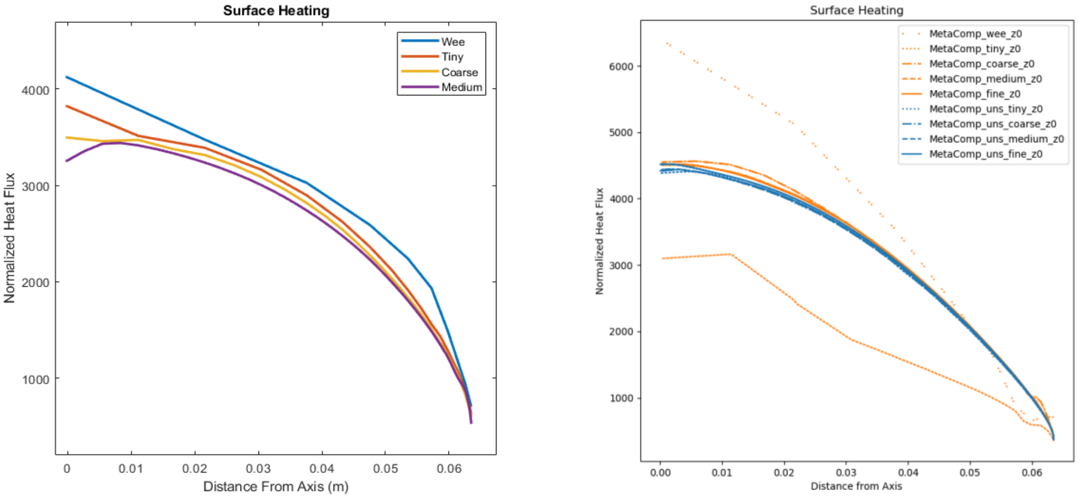

a) Present results b) Workshop results (MetaComp Tech.)

Figure 4.6 Normalized surface heat flux profiles.

The spread in the surface heating results from the workshop is quite large, but most participants obtained relatively similar results for the coarse, medium, and fine meshes. The present results seem to underpredict the surface heating towards the stagnation region at the tip of the sphere, along with some numerical instabilities in the heat flux results. However, the coarser meshes (Wee and Tiny) produced similar results to that of the finer meshes, whereas the workshop participants result for the coarser meshes were much different than the results on the finer meshes. Further analysis must be conducted to better investigate the underprediction of surface heating compared to the results from MetaComp Technologies, along with the various numerical fluctuations towards the tip of the sphere.

4.4 Conclusions

Computational simulations and results for steady laminar hypersonic flow past the Blottner Sphere are presented for five structured meshes ranging from just over 5,000 elements (the coarsest Wee mesh) to over 16 million elements (the finest mesh) provided to the participants of the 2022 High Fidelity CFD Workshop. Simulations were conducted in ANSYS Fluent with a steady, density-based solver and the laminar flow model at a freestream Mach of 5.0 and an angle of attack, α, of 0° with suitable boundary conditions. Present results predict the bow shock separated from the stagnation point of the sphere at approximately 0.0095m for all five provided meshes. The results for the normalized surface pressure profiles are within 5% of those presented by all four workshop participants (Sandia, NASA Langley, Metacomp and University of Strasburg) of the High-Fidelity CFD workshop. However, the current results under-predict the peak surface heat flux when compared to the results obtained by the other workshop participants; there is big spread among the results. Further analysis of the normalized heat flux profiles is therefore needed to allow for a deeper understanding of the surface heating to determine the reasons for differences among the present results and those among other workshop participants. Further investigation is needed in this case to make comparisons with some experimental data that utilizes the Blottner Sphere geometry and flow conditions as part of as a leading edge in a full blunt body hypersonic study.

4.5 References

[1] Davis, R. T., and Chyu W. J., “Laminar flow past a sphere at high Mach number,” Journal of Fluid Mechanics, Vol. 24, No. 3, 1966, pp. 481–495. https://doi.org/10.1017/S0022112066000764

[2] Blottner, F. G., “Accurate Navier-Stokes results for the hypersonic flow over a spherical nosetip,” Journal of Spacecraft and Rockets, Vol. 27, No. 2, 1990, pp. 113–122. https://doi.org/10.2514/3.26115

[3] Fisher, T., “High Fidelity CFD Workshop 2021: High Speed Steady Advanced Case: Blottner Sphere,” NASA Langley Research Center Turbulence Modeling Resource, 2021. https://turbmodels.larc.nasa.gov/Highfidelitycfd2021/SteadySupHypersonic_blottner_HFW_2021.pdf.

[4] Widhopf, G. F., and Hall, R., “Transitional and turbulent heat-transfer measurements on a yawed blunt conical Nosetip,” AIAA Journal, Vol. 10, No. 10, 1972, pp. 1318–1325. https://doi.org/10.2514/3.50376

[5] “Index of /HFW2022/ BlottnerSphere/Pointwise/,” Massachusetts Institute of Technology Aerospace Computational Design Laboratory, 2021, Cambridge, MA. https://acdl.mit.edu/HFW2022/BlottnerSphere/Pointwise/

[6] “Sutherland's law,” CFD Online, https://www.cfd-online.com/Wiki/Sutherland%27s_law.

Chapter 5: Summary

This thesis investigates steady hypersonic flow for two benchmark cases and compares results to other investigators from industry and academia. The geometries used for the simulations include the HIFiRE-1 test model and the Blottner Sphere, both of which have become crucial geometries for hypersonic computation and experimentation. The results are compared to those from participants from the 2022 High-Fidelity CFD workshop, along with including further simulations that offer more information on the workshop studied cases.

Results are presented for the HIFiRE-1 geometry using the Reynold-Averaged Navier-Stokes (RANS) equations with the one-equation Spalart-Allmaras (SA) turbulence model. Simulations are conducted at Mach 7.18 freestream and an angle of attack of α = 0° and 2°. Comparison of results to the High-Fidelity CFD workshop participants for the 2° angle of attack case shows that the present results are within 5% of the results reported in the workshop for the non-dimensionalized pressure and heat flux. Skin friction coefficient results were not reported by workshop participants but are presented here as a method to provide information about the wall surface shear stress within the boundary layer. The 0° angle of attack non-dimensionalized pressure results give acceptable values on both the coarse and medium meshes with trends that roughly follow those of the α = 2° case. The non-dimensionalized heat flux results for the coarse mesh depict a jagged profile, however these results closely match the general trend shown by the smooth profile from the medium mesh results. Hypersonic compressible flow is also visualized through Mach contours in the XY symmetry plane, including a detached bow shock, expansion fan, and oblique shock wave. Further investigation into the 0° angle of attack is suggested to obtain results on the finer mesh for trend verification as well as comparison to a similar ground test study experiment completed at CALSPAN University of Buffalo Research Center.

Blottner Sphere computational analysis is also completed and results are presented for steady laminar hypersonic flow on five structured meshes provided as part of the 2022 High Fidelity CFD Workshop. Mach 5.0 and 0° angle of attack freestream conditions were employed with suitable boundary conditions. Normalized surface pressure results are found to be within 5% of each of the four High-Fidelity CFD workshop participants. Normalized surface heating results from the workshop have a very large spread and the results presented here under-predict the surface heating when compared to most of the workshop participants. This large spread in surface heat flux results need to be investigated further to understand the source of the difference between the present results and those from the workshop participants. It should also be noted that there are experimental studies for the Blottner Sphere that can be used to compare and provide further insight into the heat flux results and other flow quantities of interest.